International Journal of Plasticity xxx (xxxx) xxx–xxx

Contents lists available at ScienceDirect

International Journal of Plasticity

journal homepage: www.elsevier.com/locate/ijplas

Improving ductility of a Mg alloy via non-basal < a > slip induced by Ca addition

Gaoming Zhu[a], Leyun Wang[a,*], Hao Zhou[b], Jinhui Wang[c], Yao Shen[d], Peng Tu[e], Hong Zhu[e], Wei Liu[b], Peipeng Jin[c], Xiaoqin Zeng[a,c,d,**]

[a] National Engineering Research Center of Light Alloy Net Forming, School of Materials Science and Engineering, Shanghai Jiao Tong University, Shanghai, 200240, China
[b] Nano and Heterogeneous Materials Center, School of Materials Science and Engineering, Nanjing University of Science and Technology, Nanjing, Jiangsu, 210094, China
[c] Qinghai Provincial Key Laboratory of New Light Alloys, Qinghai University, Xining, Qinghai, 810016, China
[d] State Key Laboratory of Metal Matrix Composites, Shanghai Jiao Tong University, Shanghai, 200240, China
[e] University of Michigan – Shanghai Jiao Tong University Joint Institute, Shanghai Jiao Tong University, Shanghai, 200240, China

ARTICLE INFO

Keywords:
Dislocations
Polycrystalline material
Electron microscopy
Mechanical testing
Magnesium alloy

ABSTRACT

Addition of a small amount of Ca improves the ductility of Mg alloys. However, the mechanism underlying this effect is not well understood. In this work, tensile testing of an extruded Mg – 0.47 wt% Ca alloy was conducted inside a scanning electron microscope. Electron backscattered diffraction-based slip trace analysis was performed to study in-grain slip activities at 1%, 2%, 4%, 8%, and 16% tensile strain. While the majority of the grains were deformed by $\{0001\}<11\bar{2}0>$ basal slip, slip lines from $\{1\bar{1}00\}$ prismatic planes and $\{1\bar{1}01\}$ pyramidal I planes were also frequently observed, and their fractions increased with strain. Ex situ transmission electron microscopy indicated that the pyramidal I slip lines were associated with < a > dislocations instead of < c + a > dislocations. From Schmid factor analysis, the critical resolved shear stresses of prismatic slip and pyramidal < a > slip are approximately twice that of basal slip in this Mg–Ca alloy. The enhanced activity of non-basal < a > slip improved the material's ductility. Our first-principles calculations found that solute Ca atoms would reduce the unstable stacking fault energy for all slip modes.

1. Introduction

Mg and its alloys have attracted considerable recent attention because of their low densities and high specific strengths. However, widespread usage of Mg alloys remains limited by their poor room-temperature formability. The deformation of Mg alloys at room temperature is mostly achieved by $\{0001\}<11\bar{2}0>$ basal slip and $\{10\bar{1}2\}<\bar{1}011>$ tension twinning (Stanford and Barnett, 2013; Khosravani et al., 2015), while the activation of non-basal slip modes is generally difficult.

Abbreviations: CRSS, critical resolved shear stress; DFT, density functional theory; ED, extrusion direction; GSFE, generalized stacking fault energies; ICP-AES, Inductively Coupled Plasma Atomic Emission Spectroscopy; IPF, inverse pole figure; RE, rare earth; SF, Schmid factor; SFE, stacking fault energy; SS, slip system; TBDF, two-beam dark-field; VASP, Vienna Ab-initio Simulation Package

* Corresponding author.
** Corresponding author. National Engineering Research Center of Light Alloy Net Forming, School of Materials Science and Engineering, Shanghai Jiao Tong University, Shanghai, 200240, China.
E-mail addresses: leyunwang@sjtu.edu.cn (L. Wang), xqzeng@sjtu.edu.cn (X. Zeng).

https://doi.org/10.1016/j.ijplas.2019.04.020
Received 14 July 2018; Received in revised form 9 March 2019; Accepted 28 April 2019
0749-6419/ © 2019 Elsevier Ltd. All rights reserved.

Addition of solute alloying elements into Mg is a promising approach to address the problem of poor room-temperature formability (Imandoust et al., 2017). Mg–rare earth (RE) alloys, such as Mg–Y, show much improved ductility compared to pure Mg (Sandlöbes et al., 2011, 2012; Stanford et al., 2014; Kula et al., 2016). Sandlöbes et al. (2011, 2012) reported that a Mg–3 wt.% Y sheet alloy has the tensile elongation of nearly 25% in contrast to the ~5% elongation of pure Mg sheets. Based on the transmission electron microscopy (TEM) analysis, they proposed that pyramidal < c+a > slip is a key reason for the high ductility in this alloy. Using molecular dynamics simulation, Kim et al. (2015) found that Y reduces the difference in critical resolved shear stress (CRSS) between basal slip and < c+a > slip. Most recently, Wu et al. (2018) found that Y could enhance < c+a > cross-slip between pyramidal I and pyramidal II planes, which would prevent the detrimental pyramidal-to-basal transition that is prone to happen in pure Mg (Wu and Curtin, 2015). In addition to < c+a > slip, prismatic and pyramidal < a > slips were found to be more active in Mg–Y than in pure Mg, which also contributes to the higher ductility in Y-containing Mg alloys (Huang et al., 2018; L. Wang et al., 2018b). Despite the excellent properties of Mg–RE alloys, their high cost presents a realistic obstacle for industrial application. Therefore, RE–free Mg alloys are under continuous research (Pan et al., 2016; Suh et al., 2017).

Ca is one of the most promising alloying elements for this purpose. Ca has a low solubility in Mg of about 0.43 at% (~0.71 wt%) at 517 °C (Aljarrah et al., 2008). Initially, the purpose of Ca addition was to form intermetallic compounds such as Mg_2Ca to strengthen Mg–Al and Mg–Zn alloys (Oh-ishi et al., 2009; Xu et al., 2011; Mendis et al., 2011; Seong and Kim, 2015). It was later found that dilute Ca addition could also enhance ductility. Zhang et al. (2012) developed an extruded Mg-1.0Zn-0.2Ca (wt.%) alloy (grain size = 5–20 μm) with 35.5% tensile elongation in comparison to an extruded Mg-1.0Zn (wt.%) alloy (grain size = 20–50 μm) with 16.2% tensile elongation. High ductility in Mg–Zn–Ca ternary alloys was also reported by Hofstetter et al. (2015) and Zeng et al. (2016a). Sandlöbes et al. (2017) developed a rolled Mg-1.0Al-0.1Ca (wt.%) alloy (grain size = 35–50 μm) with 20% tensile elongation. Most recently, Pan et al. (2019) fabricated an extruded Mg-1.0Ca (wt.%) binary alloy (grain size = 2 μm) with tensile elongation of 18.0%. While the high ductility in Mg–Zn–Ca ternary alloy can be attributed to texture weakening and grain refinement due to the segregation of Ca at grain boundaries (Zhang et al., 2012; Zeng et al., 2016a), the high ductility found in Mg–Al–Ca ternary alloys and Mg–Ca binary alloys suggests that Ca may intrinsically change the deformation behavior of Mg in a similar way as some rare earth elements. In fact, Sandlöbes et al. (2017) observed an increased activity of < c+a > slip in the deformed Mg–1Al–0.1Ca alloy. This is consistent with the molecular dynamics (MD) calculation by Kim et al. (2018) who found that Ca atoms have higher dislocation binding energy and solid solution strengthening on basal < a > slip than on < c+a > slip. Using density functional theory (DFT), Yasi et al. (2012) calculated the interaction between different solute atoms and screw < a > dislocation and predicted that Ca could promote basal-to-prismatic cross-slip in Mg. Considering these different interpretations, further experimental analysis of the effect of Ca on the deformation behavior of Mg is necessary.

Compared to TEM that usually focuses on the dislocation characteristics in only a few grains, electron backscattered diffraction (EBSD) with slip trace analysis allows a more statistical study of the slip activities among a large number of grains. Using this method, Cepeda-Jiménez et al. (2015, 2018) studied the influence of grain size and testing temperature on the relative activity of basal, prismatic, and pyramidal < c+a > slip modes in various Mg alloys to understand the difference in material ductility. Li and Boehlert (2013) developed a statistical approach to estimate the CRSS ratio of different slip modes in hexagonal Ti alloy. Commercial or custom-made test modules can be placed within scanning electron microscopes (SEM) for in situ tests that would allow slip trace analysis when the specimen is under a certain amount of strain (Barkia et al., 2015; Boehlert et al., 2012; H. Wang et al., 2016). Nonetheless, few works have tracked the relative activity of different slip modes at different strains.

In this work, the deformation of a Mg–0.47 wt% Ca alloy was studied by an in situ tensile test inside an SEM equipped with an EBSD system. The slip activities of different slip modes were analyzed by slip trace analysis at five different strain levels. At the beginning of the plastic stage (strain = 1%), the deformation was dominated by basal slip. Prismatic, pyramidal I < a > slip, and pyramidal II < c+a > slip were found active in later deformation. The influence of grain orientation and Schmid factor on the choice of active slip mode and the amount of shear by different slip modes were further assessed. Non-basal < a > slips in this Mg–Ca alloy are apparently more active than those in Mg–Nd and AZ31 alloys. First-principle calculations were employed to understand how Ca atoms modify the deformation behavior in Mg.

2. Methods

2.1. Experimental procedure

Commercial-purity Mg (99.95%) and a Mg–20 wt% Ca master alloy were used to prepare the Mg–Ca alloy by casting at 730 °C. Chemical composition of the cast billet was found to be Mg–0.47 wt% Ca using Inductively Coupled Plasma Atomic Emission Spectroscopy (ICP-AES). The cast billet was solution treated at 400 °C for 24 h, then extruded at 350 °C (extrusion ratio = 18:1, extrusion speed = 2 mm/s). The as-extruded material was examined by synchrotron X-ray diffraction at Shanghai Synchrotron Radiation Facility (Yang et al., 2015) to examine the initial texture and potential secondary phases. The sample for the X-ray characterization was 1 mm thick; X-ray with the energy of 18 keV was transmitted through it to generate diffraction signals, which were recorded by a two-dimensional X-ray detector (Mar225). Tensile specimens were fabricated from the as-extruded material by electron discharge machining into a flat dog-bone shape. The gauge of each specimen is 11.0 mm (L) × 4.0 mm (W) × 1.4 mm (T). The length of the gauge is parallel to the extrusion direction. The top surface of each specimen was mechanically ground and electropolished in an ethanol–10% perchloric acid electrolyte at 30 V and −30 °C for 150 s for EBSD characterization.

The specimen was then mounted in a MICROTEST 200N (Deben, UK) module placed in a Zeiss Gemini SEM with an EBSD system (Oxford Instrument, UK). The test was conducted at a crosshead speed of 0.1 mm min^{-1}, equivalent to the nominal strain rate of

$1.5 \times 10^{-4}\,s^{-1}$. The crosshead displacement was continuously recorded during the test for estimating the instantaneous strain in the specimen. The test was paused at the tensile strains of 1%, 2%, 4%, 8%, and 16% to allow EBSD data acquisition and secondary electron imaging for the same surface region. The EBSD data was analyzed by OIM™ software (EDAX Inc., USA). Slip trace analysis was performed for the observed slip lines at each deformation step. A set of parallel slip lines in a given grain is associated with dislocation movement on a particular slip plane. These slip lines should be parallel to the intersection line between the slip plane and the sample surface. Based on the grain orientation measured by EBSD, we could compute the directions of all possible slip planes in the sample coordinate system and draw their intersections with the surface plane. Comparing the computational result with the observed slip lines allowed us to infer the activated slip system. Note that this method is limited in that it only provides information about the slip plane of the active slip system. If a slip plane contains more than one possible slip directions, the active slip system has to be determined based on certain assumption. Specifically, if basal slip lines are identified, the one with the highest Schmid factor among the three basal slip systems is assumed to be active. A more complicated situation is when slip lines are associated with pyramidal I planes $\{1\bar{1}01\}$, on which both < a > slip and < c+a > slip can occur. TEM is required to determine the dislocation type (i.e., < a > or < c+a >). A lifted-out TEM sample from a grain with $\{1\bar{1}01\}$ slip lines was prepared using a focused ion beam (FIB) instrument (GAIA3 Model, 2016; Tescan, Czech Republic). The dislocations in this grain were imaged by TEM (Talos F200X, FEI, USA) and their Burges vector could be determined using the invisibility criterion. More TEM samples were prepared by conventional twin-jet polishing to randomly select grains and identify the internal dislocations using a JEOL JEM–2100F instrument. The purpose is to draw a statistical picture of the relative percentage of < a > and < c+a > dislocations at different strain levels.

2.2. First-principles calculation

To study the influence of Ca addition on the dislocation activity in Mg, the generalized stacking fault energy (GSFE) curves of different slip systems are calculated by DFT within the Vienna Ab-initio Simulation Package (VASP). The ion–electron interaction is determined using the projector augmented wave method. The exchange-correlation function is described by the generalized gradient approximation of Perdew–Burke–Ernzerhof. To calculate the GSFE curve for a slip system, a 12-layer supercell is established, with the layers being parallel to the slip plane. Each layer contains 2×2 atoms. A 15 Å vacuum is inserted between periodically repeated supercells to avoid artificial interaction between adjacent supercells. For pure Mg, the GSFE curve can be calculated by shifting the upper half of the supercell with respect to the lower half along the slip direction. In the case of Mg–Ca, one Mg atom in the 6th layer near the stacking-fault plane is replaced by a Ca atom, corresponding to a doping concentration of 1/48 = 2.1 at.% Ca.

The unstable SFE (γ_{us}) is obtained as the saddle point on the GSFE curve. More details regarding the GSFE calculation can be found in Dong et al. (2018).

3. Results

3.1. Microstructure and texture

Fig. 1(a) shows a synchrotron radiation X-ray diffraction pattern of the as-extruded material. The diffraction pattern comprises

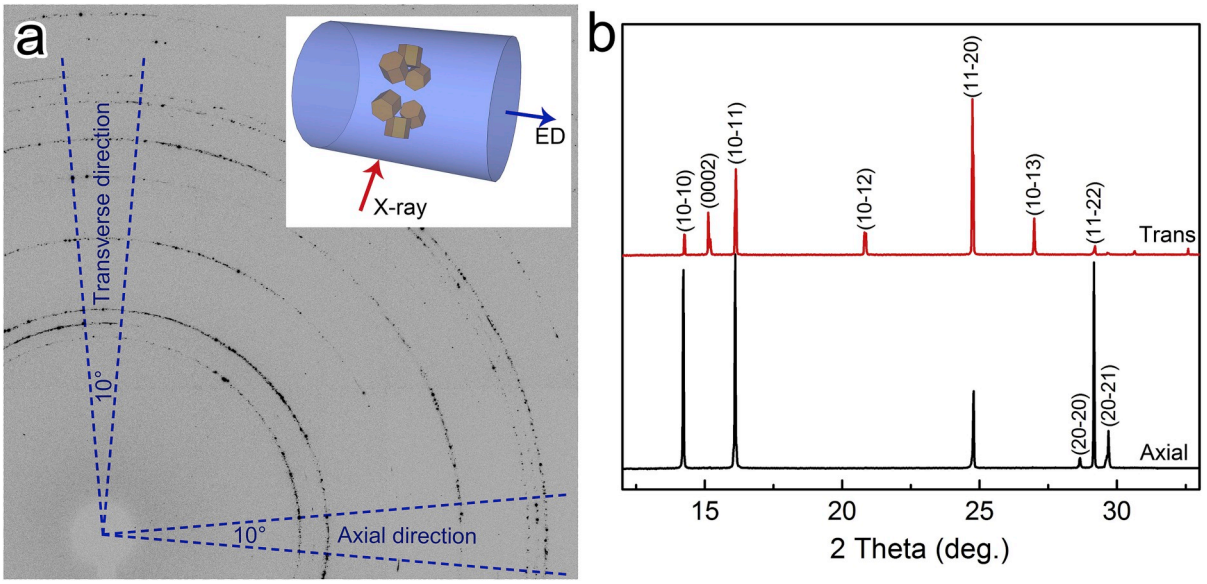

Fig. 1. (a) Synchrotron X-ray diffraction pattern of the as-extruded Mg–Ca alloy; (b) integrated diffraction profiles around the axial and transverse directions.

several Debye diffraction rings, which is typical for polycrystals. In the diffraction pattern, the axial direction is parallel to the extrusion direction (tensile direction), and the transverse direction is perpendicular to both the tensile direction and the beam direction. The two-dimensional diffraction pattern is integrated into one-dimensional diffraction profiles (Fig. 1(b)) over 0 ± 5° (axial direction) and 90 ± 5° (transverse direction) ranges using the software Fit2D. In both profiles, only the diffraction peaks from the Mg phase are identified, indicating the absence of secondary phases (such as Mg_2Ca) at this low concentration of 0.47 wt% Ca. This is consistent with the literature (Gu et al., 2009). In Fig. 1(b), the peak intensity in the axial profile is unlike that in the transverse profile. In particular, the (0002) peak present in the transverse profile is barely observable in the axial profile, which is expected for an extruded Mg alloy. This result, along with the {0002} pole figure by EBSD in Fig. 2(j) implies that Ca does not dramatically alter the extrusion texture as some RE element do (Imandoust et al., 2017). The result here is consistent with the work by Zeng et al. (2016b) in that the texture weakening effect was observed only in Mg–Zn–Ca ternary alloys but not in Mg–Ca binary alloys.

3.2. In situ tensile test

Fig. 2(a) shows the inverse pole figure (IPF) map of a region near the center of the specimen surface, as obtained by EBSD before deformation in relation to the tensile axis. This region contains 753 grains, and subsequent slip trace analysis focuses on this region. Most grains show colors of green or blue, indicating that their c-axes are nearly perpendicular to the tensile axis. The IPF map reveals a near-equiaxed and twin-free grain structure with a mean grain size of ~35 μm. Fig. 2(b) shows the stress–strain curve from the in situ tensile test. The specimen failed at approximately 18% strain. The glitches in the stress–strain curve are caused by stress relaxation during pauses at different strains. Note that the reloading at each step beyond 4% strain would require a slightly higher stress than the initial flow stress. This phenomenon known as strain aging was found in Fe–C (Cottrell et al., 1949) and Al–Mg systems (Aboulfadl et al., 2015). Strain aging has been shown to be related to solute binding of dislocations (i.e. the segregation of solute atoms to form atmospheres around dislocations). The observation of strain aging in this alloy suggests that Ca atoms could also be attracted to dislocations in the Mg lattice. Segregation of Ca atoms to basal < a > dislocations was directly observed using a correlative transmission electron microscopy and atom probe tomography (TEM-APT) by Bian et al. (2018) in a Mg–Al–Zn–Mn–Ca alloy. At each paused step, secondary electron images and EBSD scans were obtained from the same region as that shown in Fig. 2(a). IPF maps of a more confined area at different strains are shown in Fig. 2(c–h). As the strain is increased, some grains develop large orientation gradients (e.g., Grain 23 and Grain 25), while other grains show some twinning activity (e.g., Grain 20 and Grain 43). Slip lines are observed after deformation, as shown by the secondary electron image obtained from this region after 8% strain in Fig. 2(i). Fig. 2(j) shows the {0002} pole figures corresponding to the large area of Fig. 2(a) at 0 and 16% strains. The change in the {0002} pole distribution is relatively small during the tensile test.

The total volume of twins was calculated using the image-processing software Image-Pro 6.0. Fig. 3 shows the evolution of the twin volume fraction and the number of grains with twins at different strains. The twin volume fraction is increased almost linearly with strain. The number of grains with twins is increased more rapidly in the early deformation stage (0%–4% strain) than in the later stage (4%–16% strain), indicating that twin nucleation mostly occurs during early deformation. The increase of the twin volume fraction in later-stage deformation is mostly due to twin growth. Twin growth in Grain 52 where two twin variants have developed is shown in Fig. 3.

Although the twin volume fraction was increased with strain, its value was only 1.0% at 4% strain. This is mainly because of the extrusion texture, which is unfavorable for twin nucleation. For comparison, a similar tensile experiment was performed for extruded alloys of Mg–2 wt.% Nd (extruded at 500 °C) and AZ31 (extruded at 350 °C, followed by annealing at 500 °C for 1h) whose grain sizes are similar as the Mg–0.47 wt% Ca alloy. After 4% tensile strain, the twin volume fractions in these two alloys were 4.5% and 2.3%, respectively. Thus, it can be concluded that twinning has a negligible effect on the deformation of this Mg–Ca alloy. The high ductility of the alloy must be associated with the dislocation activities, which is studied next.

3.3. Statistical analysis of slip activity

Slip trace analysis was performed using a self-developed code (L. Wang et al., 2011) for all grains in the region of Fig. 2(a) where surface slip lines are observed. Fig. 4 illustrates the practice of slip trace analysis in four grains (i.e., Grains 24, 22, 29, and 53 as marked in Fig. 2), where different types of slip lines are developed at different strains. The theoretical slip trace directions for the following slip systems (SS) are computed using the grain orientation information of each grain: SS 1–3 for basal slip, SS 4–6 for prismatic < a > slip, SS 7–12 for pyramidal I < a > slip, and SS 13–18 for pyramidal II < c + a > slip. The Schmid factors (SF) of these slip systems are also computed under the condition of uniaxial tension and given in Table 1. For Grain 24, the slip lines (marked by a red line) are observed on the surface after 4% strain and become denser at higher strains. As shown in Fig. 4(a), these slip lines are parallel with the theoretical basal slip trace (SS 1–3 having the same slip plane). Among the three basal slip systems, $(0001)[\bar{1}2\bar{1}0]$ with the highest SF of 0.34 is assumed to be the activated slip system in Grain 24. For Grain 22, the slip lines first become visible in its upper part after 4% strain (marked by a blue line). As shown in Fig. 4(b) and Table 1, they correspond to the activation of $(\bar{1}100)[\bar{1}\bar{1}20]$ (SS 6) with a SF of 0.42. When the strain is increased to 8%, another set of slip lines corresponding to the activation of $(10\bar{1}0)[\bar{1}2\bar{1}0]$ (SS 5) with a SF of 0.44 is observed. Grain 22 is an example of multiple slip systems becoming active in one grain. For Grain 29, slip lines are visible after 8% strain (marked by a green line). As shown in Fig. 4(c) and Table 1, they seem to be caused by the activation of $(\bar{1}011)[\bar{1}2\bar{1}0]$ (SS 8). Alternatively, pyramidal I < c + a > slip, $(\bar{1}011)[11\bar{2}3]$ or $(\bar{1}011)[2\bar{1}\bar{1}3]$, may also be responsible for these slip lines.

In order to clarify whether the observed pyramidal I slip lines belong to < a > or < c + a > slip, we deformed another specimen

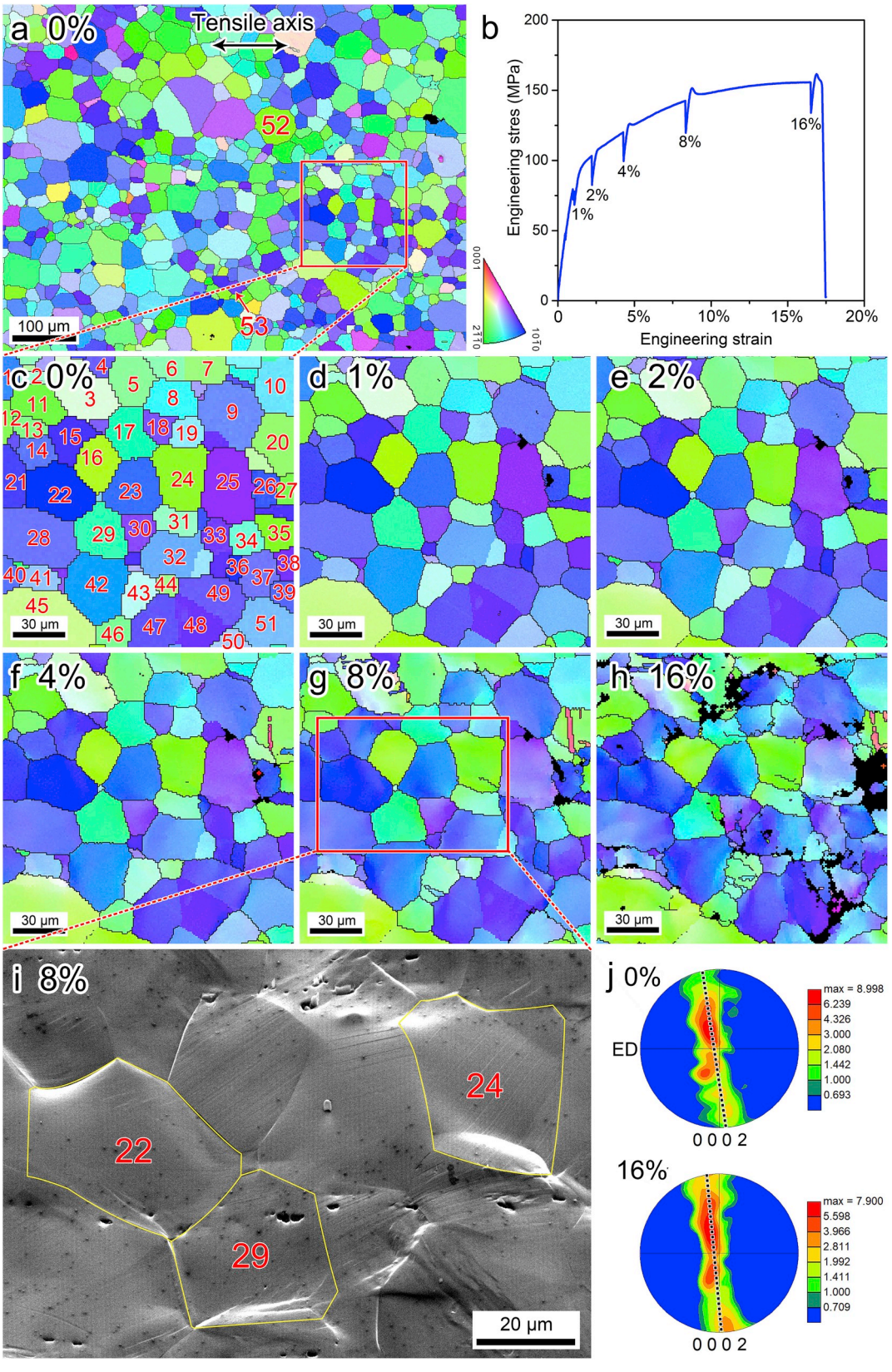

(caption on next page)

Fig. 2. (a) IPF map of a surface region of the specimen prior to deformation relative to the tensile axis; (b) stress–strain curve of the in situ tensile test; (c–h) IPF maps of the outlined area from (a) at different strains; (i) secondary electron image taken after 8% strain; (j) {0002} pole figures corresponding to the large area in Fig. 2(a) at 0 and 16% strains.

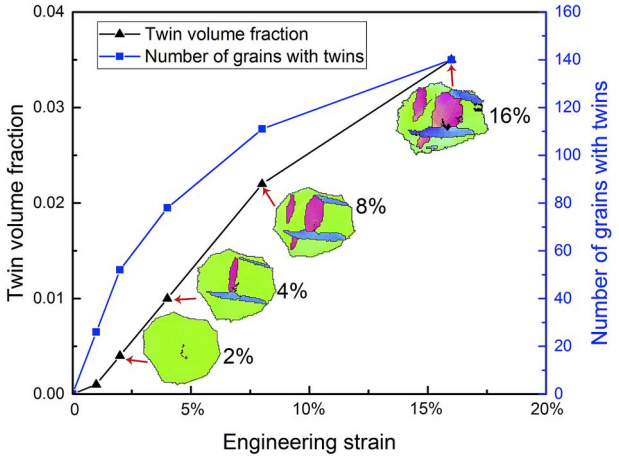

Fig. 3. Twin volume fraction and number of grains with twins at different tensile strains. Twin growth in Grain 52 where two twin variants have developed is also shown.

by 4% strain and chose a grain with apparent pyramidal I slip lines for dislocation Burgers vector analysis. A TEM thin foil was extracted from the pyramidal slip region using FIB, as shown in Fig. 5(a−c). Subsequent dislocation analysis by the invisibility criterion ($\boldsymbol{g}\cdot\boldsymbol{b} = 0$) reveals that the TEM foil contains < a > dislocations rather than < c + a > dislocations, as dislocations are visible under $\boldsymbol{g} = (2\bar{1}\,\bar{1}0)$ but invisible under $\boldsymbol{g} = (0002)$ (Fig. 5(d and e)). This experiment indicates that the pyramidal I slip lines in this grain were caused by < a > slip. For Grain 53, slip lines are observed after 8% strain. These slip lines are best matched by the slip trace of $(\bar{1}\bar{1}22)[\bar{1}\bar{1}2\bar{3}]$ (SS17), a pyramidal II < c + a > slip system.

Further ex-situ TEM studies were conducted to estimate the fraction of < a > and < c + a > dislocations at different strain levels. Dislocation analysis was performed in a total of 46 grains: 9 grains from a specimen deformed by 1% strain, 13 grains from a specimen deformed by 2% strain, 8 grains from a specimen deformed by 4% strain, and 16 grains from a specimen deformed by 8% strain. In most of the 46 grains, only < a > dislocations were observed; < c + a > dislocations were observed in only 5 grains from the specimen deformed by 8% strain, and they are often accompanied by < a > dislocations in the vicinity. Fig. 6 shows an example: < c + a > dislocations are visible under both $\boldsymbol{g} = (10\bar{1}0)$ and $\boldsymbol{g} = (0002)$, while < a > dislocations become invisible under $\boldsymbol{g} = (0002)$. This finding agrees with the literature in that < c + a > dislocations become active only after a critical strain is exceeded (Sabat et al., 2018).

Those TEM works suggest that while < c + a > slip can occur on pyramidal II planes, the observed pyramidal I slip lines are more likely from < a > dislocations than from < c + a > dislocations. This hypothesis is also supported by SF analysis. Pyramidal I slip lines were observed in a total of 25 grains in the investigated area after 4% strain. The maximum SFs for the six $\{10\bar{1}1\} < \bar{1}2\bar{1}0 >$ systems and the twelve $\{10\bar{1}1\} < 11\bar{2}\bar{3} >$ systems were computed for the 25 grains, as shown in Fig. 7. It turns out that *all* of them have higher SFs for pyramidal I < a > slip than for pyramidal I < c + a > slip. Because the nucleation of < c + a > dislocations is usually more difficult than that of < a > dislocations, these grains are more likely deformed by pyramidal I < a > slip than by pyramidal I < c + a > slip. For the above reasons, the observed pyramidal I slip lines will be marked as pyramidal I < a > slip in the following analysis.

Fig. 8 shows the slip trace analysis result for the area of Fig. 2(g). After 8% strain, the majority of the slip lines still belong to basal slip. Prismatic slip lines are found in Grains 17, 21, 22, and 32; pyramidal I slip lines are found in Grains 1, 13, 25, 29, and 45. While slip lines in Grains 25 and 32 approximately match pyramidal II slip trace, these slip lines also match pyramidal I < a > slip trace or prismatic slip trace. In both grains, Schmid factor of the < a > slip systems are higher than that of the pyramidal II < c + a > slip systems. Therefore, slip lines in these two grains are attributed to pyramidal I < a > slip and prismatic slip. Instant grain orientations of Grains 1–51 after 8% strain are given in the Supplementary Data.

Slip trace analysis was further performed for all 753 grains within the surface region in Fig. 2(a). After the tensile test, slip lines are visible in 39, 97, 149, 192, and 218 grains after 1%, 2%, 4%, 8%, and 16% strains, respectively. Fig. 9 and Table 2 show the statistics of the identified slip activities. Note if a grain developed more than one type of slip lines, then each type is counted once in Table 2. For comparison, slip trace analysis was also performed for the Mg–2 wt.% Nd and AZ31 specimens after 4% tensile strain. In the Mg–0.47 wt% Ca specimen, basal slip accounts for 85.7% of the observed slip lines at 1% strain. As the strain is increased, more grains develop non-basal slip traces. For example, 28.2% of the slip lines belong to either prismatic or pyramidal I < a > slip after 4% strain. For Mg–2 wt.% Nd and AZ31 after 4% strain, the fractions of non-basal slip lines are only 7.8% and 10.7%, respectively. The comparison clearly indicates that non-basal slip is more active in the Mg–0.47 wt% Ca alloy than it is in Mg–2 wt.% Nd and AZ31.

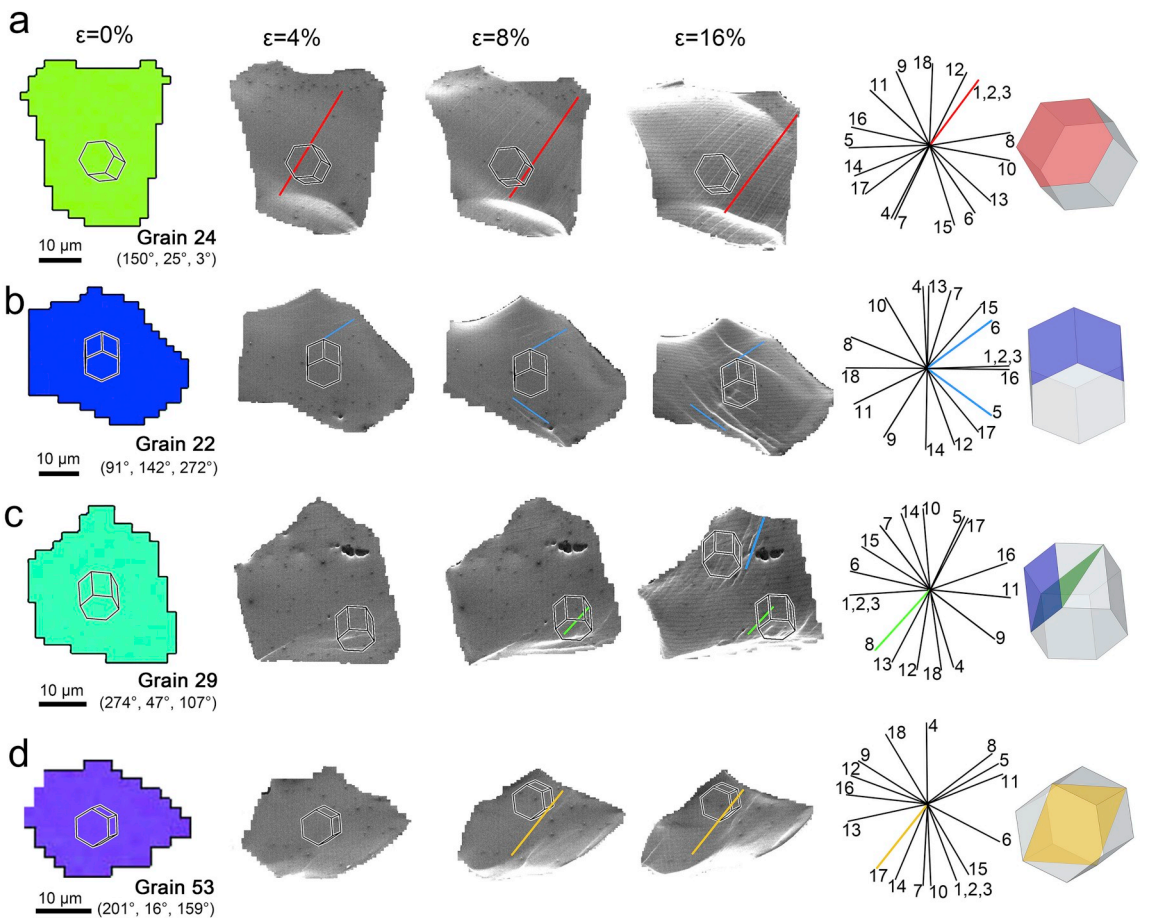

Fig. 4. Slip trace analyses for four grains where slip lines are developed from 4% to 16% strains. (a) Grain 24 shows basal slip trace; (b) Grain 22 shows prismatic slip trace; (c) Grain 29 shows pyramidal I slip trace; (d) Grain 53 shows pyramidal II slip traces. The theoretical slip trace directions shown on the right are computed using the grain orientations at 8% strain. The slip plane(s) of the identified active slip system(s) are highlighted in the hexagonal unit cell of each grain.

Table 1
Calculated Schmid factors of the eighteen slip systems in Grains 24, 22, 29, and 53. SFs of the activated slip system(s) are bolded for each grain.

Slip mode	SS	Slip plane	Slip direction	Schmid factors			
				Grain 24	Grain 22	Grain 29	Grain 53
Basal < a > slip	1	(0001)	$[2\bar{1}\bar{1}0]$	0.17	0.00	0.02	0.00
	2	(0001)	$[\bar{1}2\bar{1}0]$	**0.34**	0.01	0.03	0.21
	3	(0001)	$[\bar{1}\bar{1}20]$	0.17	0.01	0.05	0.21
Prismatic < a > slip	4	$(01\bar{1}0)$	$[2\bar{1}\bar{1}0]$	0.37	0.02	0.32	0.01
	5	$(10\bar{1}0)$	$[\bar{1}2\bar{1}0]$	0.01	**0.44**	0.49	0.41
	6	$(\bar{1}100)$	$[\bar{1}\bar{1}20]$	0.38	**0.42**	0.18	0.40
Pyramidal I < a > slip	7	$(01\bar{1}1)$	$[2\bar{1}\bar{1}0]$	0.25	0.02	0.27	0.01
	8	$(\bar{1}011)$	$[\bar{1}2\bar{1}0]$	0.15	0.40	**0.42**	0.46
	9	$(1\bar{1}01)$	$[\bar{1}\bar{1}20]$	0.25	0.38	0.13	0.45
	10	$(10\bar{1}1)$	$[\bar{1}2\bar{1}0]$	0.41	0.02	0.29	0.01
	11	$(\bar{1}101)$	$[\bar{1}\bar{1}20]$	0.17	0.39	0.45	0.26
	12	$(0\bar{1}11)$	$[2\bar{1}\bar{1}0]$	0.42	0.37	0.18	0.25
Pyramidal II < c+a > slip	13	$(2\bar{1}\bar{1}2)$	$[2\bar{1}\bar{1}\bar{3}]$	0.04	0.00	0.06	0.03
	14	$(11\bar{2}2)$	$[11\bar{2}\bar{3}]$	0.12	0.34	0.45	0.19
	15	$(\bar{1}2\bar{1}2)$	$[\bar{1}2\bar{1}\bar{3}]$	0.48	0.32	0.20	0.18
	16	$(\bar{2}112)$	$[\bar{2}11\bar{3}]$	0.11	0.00	0.04	0.03
	17	$(\bar{1}\bar{1}22)$	$[\bar{1}\bar{1}2\bar{3}]$	0.04	0.35	0.41	**0.39**
	18	$(1\bar{2}12)$	$[1\bar{2}1\bar{3}]$	0.17	0.33	0.17	0.37

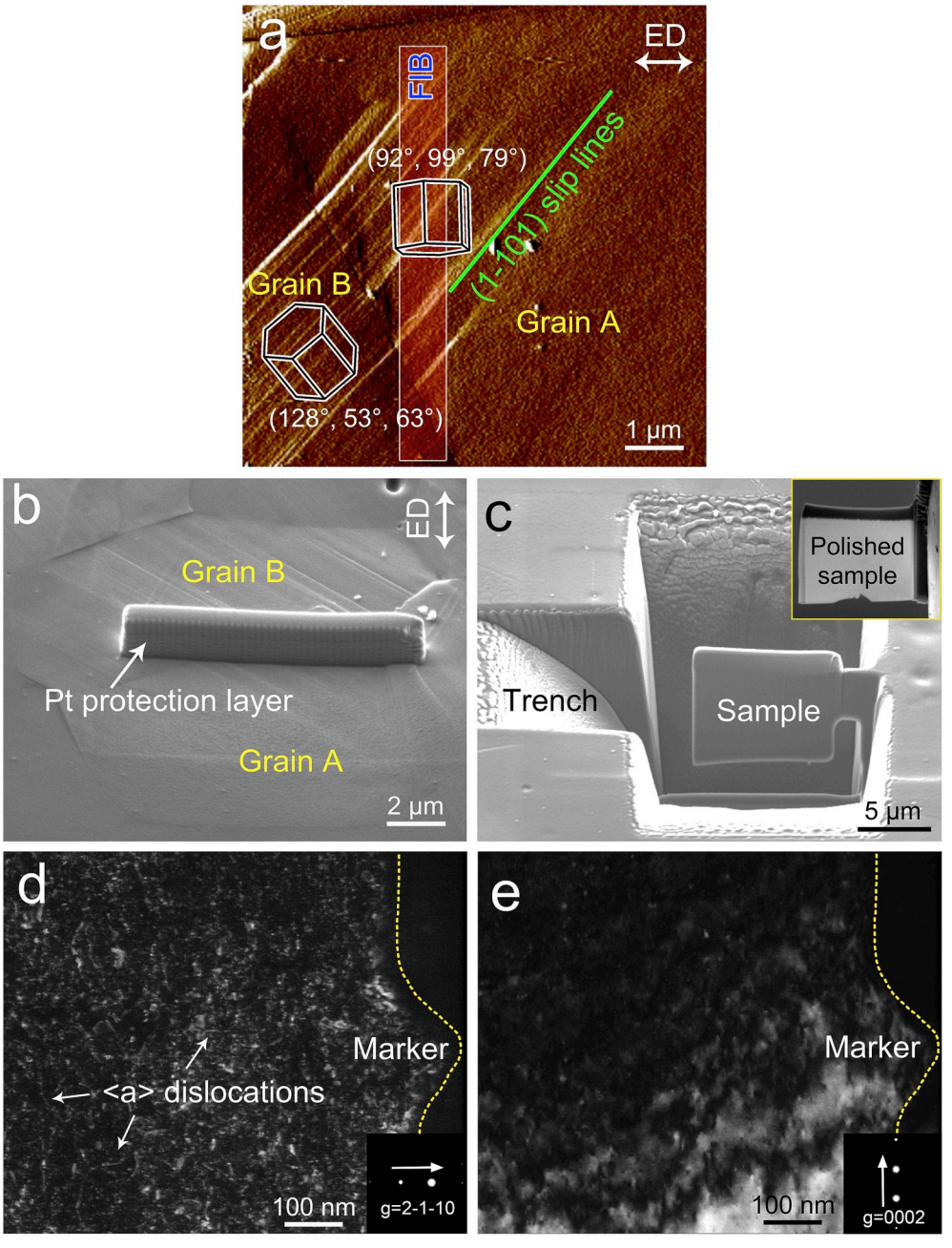

Fig. 5. Identification of the dislocations associated with pyramidal I slip lines in a specimen after 4% strain. (a) Pyramidal I slip lines are identified in Grain A whose orientation (in Euler angles) is shown. A TEM thin foil across these slip lines was extracted by FIB. (b) The location of the thin foil to be lifted out. (c) After FIB cutting of a large trench, the foil emerged and was extracted using a microprobe. (d, e) Two-beam dark-field images taken along the $[10\bar{1}0]$ zone axis under $\boldsymbol{g} = (2\bar{1}\bar{1}0)$ and $\boldsymbol{g} = (0002)$, respectively.

Fig. 10 compares the {0002} pole figures of the Mg–Ca, Mg–Nd, and AZ31 alloys after extrusion and heat treatment. Texture in the Mg–Nd alloy is apparently weaker than the other two. With more grains having favorable orientation for basal slip, the Mg–2 wt. % Nd alloy has a higher fraction of basal slip than both Mg–Ca and AZ31, as shown in Fig. 9. This also results in high tensile elongation (~17%) but low UTS (137 MPa) of the Mg–2 wt.% Nd alloy. A more interesting comparison is between Mg–Ca and AZ31. These two alloys show typical extrusion texture with similar texture strength. Nevertheless, the Mg–0.47 wt% Ca alloy shows tensile elongation (~18%) almost twice of that in AZ31 (~7%). This must be attributed to the more active non-basal slip due to the presence of Ca.

In Mg alloys, the ratio of CRSS for non-basal versus basal slip ($CRSS_{non\text{-}basal}/CRSS_{basal}$) is an important factor that influences

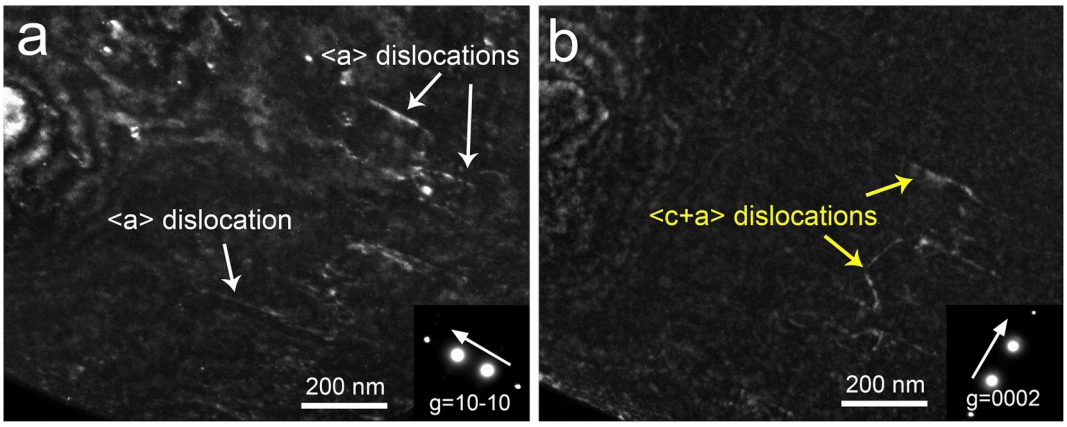

Fig. 6. In a specimen deformed by 8% strain, < c + a > dislocations were identified in a grain based on the invisibility criterion; < a > dislocations were also found in their vicinity.

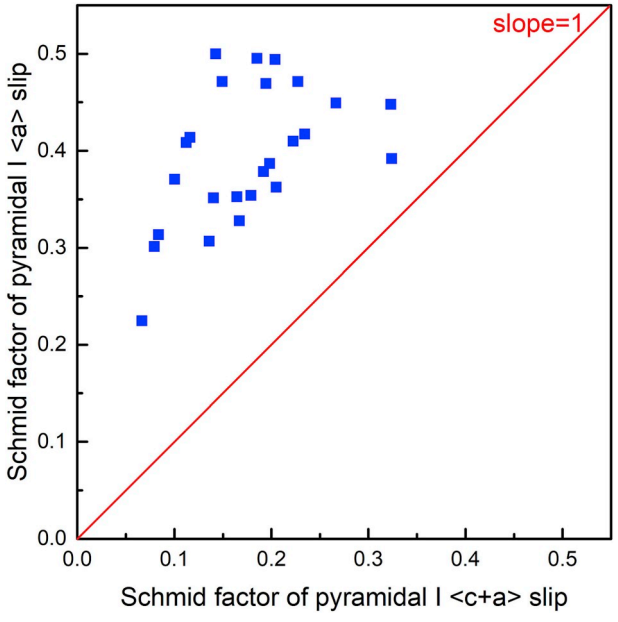

Fig. 7. Schmid factors for pyramidal I < c + a > slip and pyramidal I < a > slip for the 25 grains with pyramidal I slip traces after 4% strain.

material ductility. For a given grain, if non-basal and basal slip lines are observed concurrently during early deformation, the ratio of $CRSS_{non\text{-}basal}/CRSS_{basal}$ is approximately equal to the ratio of $SF_{non\text{-}basal}/SF_{basal}$. Using this approach, the SFs of basal slip and non-basal slip are calculated for all grains with slip traces. Fig. 11(a) shows the SFs of $\{0001\} < \bar{1}2\bar{1}0 >$ basal slip and $\{10\bar{1}0\} < \bar{1}2\bar{1}0 >$ prismatic slip for those grains with basal or prismatic slip traces at the strain of 2%. For grains with basal slip traces, the highest SF values for $\{0001\} < \bar{1}2\bar{1}0 >$ basal slip and $\{10\bar{1}0\} < \bar{1}2\bar{1}0 >$ prismatic slip are used in the figure. For grains with prismatic slip traces, the highest SF value for $\{0001\} < \bar{1}2\bar{1}0 >$ basal slip and the SF of the identified prismatic slip system (by slip trace analysis) are used in the figure.

As shown in Fig. 11(a), grains with prismatic traces show medium-to-high SF (0.3–0.5) for prismatic slip and low SF (0–0.2) for basal slip; grains with basal traces show widely distributed SF (0.1–0.5) for basal slip and medium-to-high SF (0.3–0.5) for prismatic slip. These two populations can be separated by two lines passing the origin point: line 1 with the slope of 1.9 and line 2 with the slope of 2.6. 15/16 (93.8%) grains with prismatic traces are to the left of line 1, while 63/67 (94.0%) grains with basal slip traces are to the right of line 2. Thus, it is estimated that the ratio of $CRSS_{prism}/CRSS_{basal}$ is between 1.9 and 2.6 under the assumption that the stress state in these grains were similar as the applied uniaxial tension. Similarly, it is estimated that the ratio of $CRSS_{pyr\ I < a >}/CRSS_{basal}$ is between 1.8 and 2.4, as illustrated in Fig. 11(b).

Whether a grain develops basal slip or non-basal slip is dependent on its orientation, particularly the angle between its c-axis and

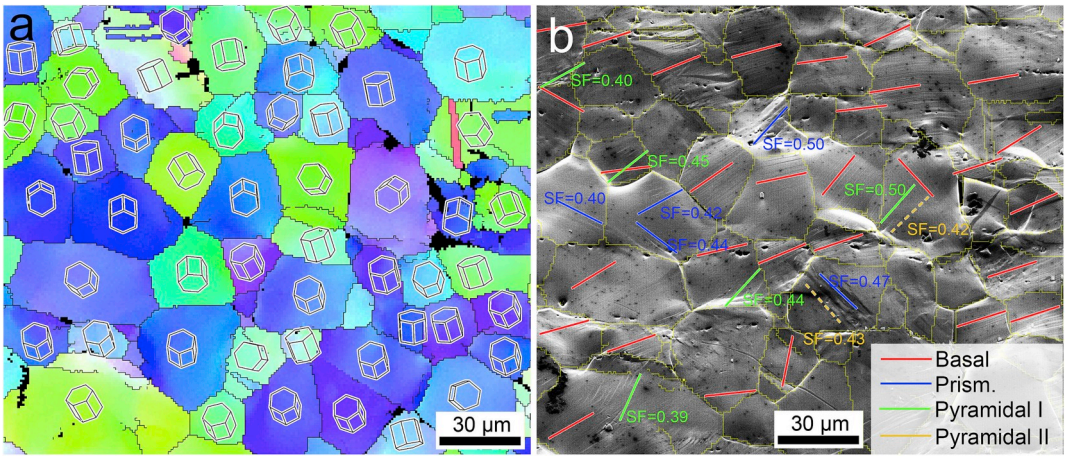

Fig. 8. Slip trace analysis for the area in Fig. 2(g) after 8% strain. The grain orientations are represented by hexagonal unit cells in (a), and the slip lines are identified in individual grains in (b).

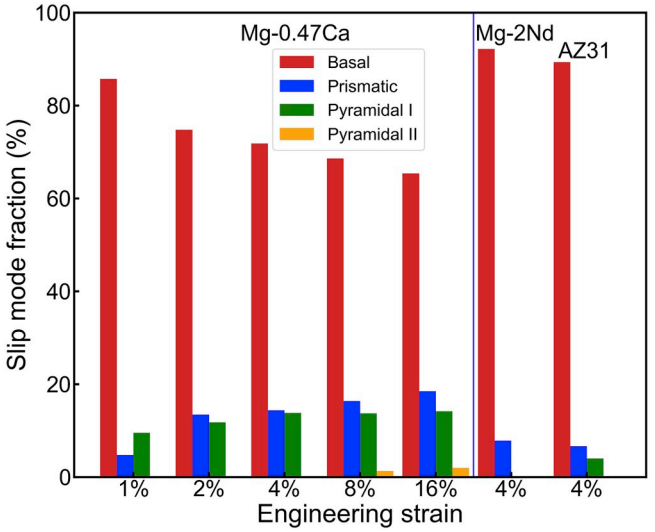

Fig. 9. Statistics of the identified slip activity at different strains for the Mg–0.47 wt% Ca, Mg–2 wt.% Nd, and AZ31 specimens.

Table 2
Mechanical properties and identified twin and slip activities for the Mg–0.47 wt% Ca, Mg–2 wt.% Nd, and AZ31 specimens at various strains.

Materials	Grain size (μm)	UTS[a] (MPa)/Elongation	Strain	Twin volume fraction	Slip traces (number/fraction)			
					Basal	Prismatic	Pyramidal I	Pyramidal II
Mg–0.47 wt% Ca	35	162/18%	1%	0.1%	36/85.7%	2/4.8%	4/9.5%	0/0
			2%	0.4%	89/74.8%	16/13.4%	14/11.8%	0/0
			4%	1.0%	130/71.8%	26/14.4%	25/13.8%	0/0
			8%	2.2%	155/68.6%	37/16.4%	31/13.7%	3/1.3%
			16%	3.5%	166/65.4%	47/18.5%	36/14.2%	5/2.0%
Mg–2 wt.% Nd	43	137/17%	4%	4.5%	94/92.2%	8/7.8%	0/0	0/0
AZ31	46	208/7%	4%	2.3%	67/89.3%	5/6.7%	3/4.0%	0/0

[a] UTS: Ultimate tensile strength.

the tensile direction, θ_c. Fig. 12 shows the fraction of grains with slip traces for different θ_c values at 16% strain. Slip traces from different slip modes are also differentiated in figure. If multiple slip modes are observed in one grain, the grain is counted for each slip mode category. From Fig. 12, grains with θ_c within 30–70° almost exclusively contain basal slip traces. Grains with θ_c greater than 70° show more significant presences of prismatic or pyramidal slip traces. When the c-axis of a grain is nearly perpendicular to the tensile axis, the SF of basal slip is small, facilitating the activation of non-basal slip systems.

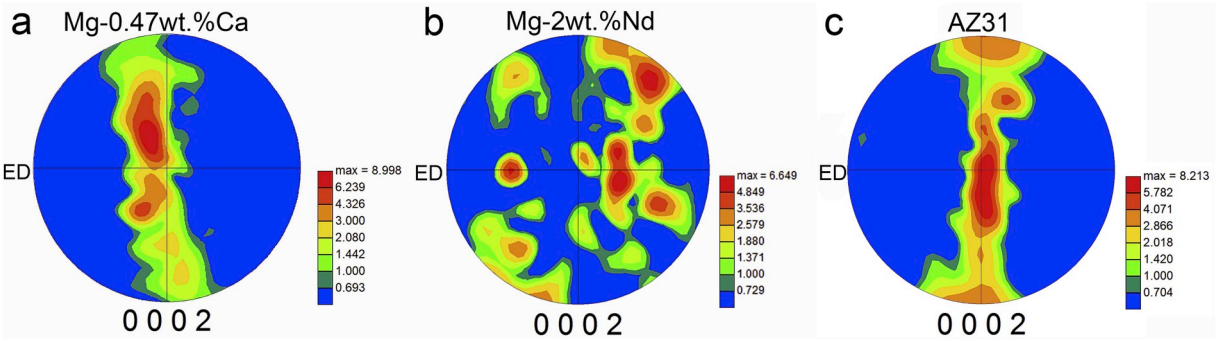

Fig. 10. {0002} pole figures of the Mg–0.47 wt% Ca, Mg–2 wt.% Nd, and AZ31 alloys after extrusion and heat treatment.

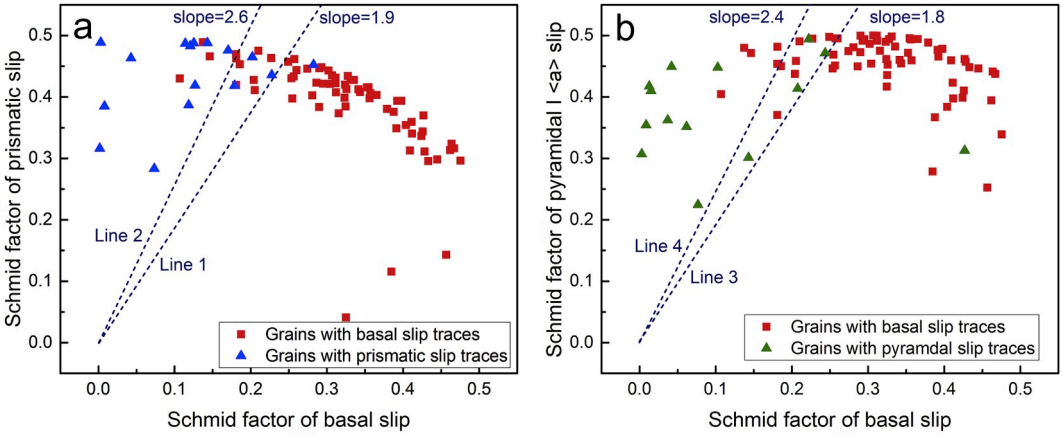

Fig. 11. (a) Schmid factors of basal slip and prismatic slip for grains with basal or prismatic slip traces at 2% strain; (b) Schmid factors of basal slip and pyramidal I < a > slip for grains with basal or pyramidal I slip traces at 2% strain.

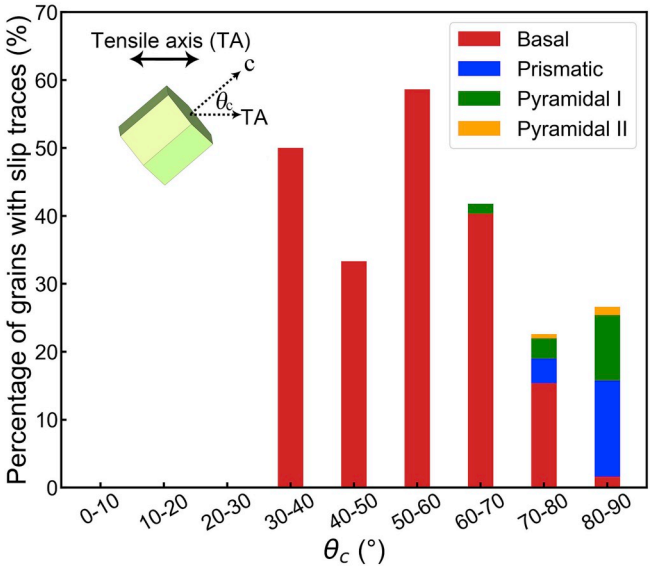

Fig. 12. Percentage of grains with slip traces for grains with different θ_c values at the strain of 16%. Slip traces from basal, prismatic, pyramidal I and II planes are also differentiated.

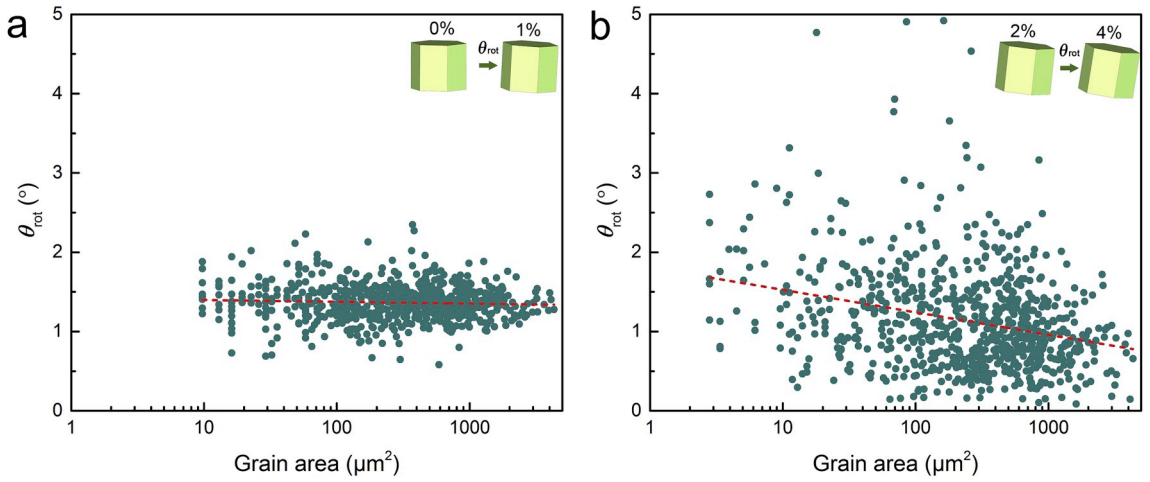

Fig. 13. Distribution of θ_{rot} with respect to the grain area measured for: (a) 706 grains from 0% to 1% strain, (b) 770 grains from 2% to 4% strain.

3.4. Statistical analysis of grain rotation

The observation of slip lines indicates the activation of corresponding slip systems in the corresponding grains. However, the amount of plastic deformation associated with each slip mode may or may not be the same. The in situ EBSD data allows us to quantitatively investigate this question by following the orientation rotation of each grain. We define the value of grain rotation (θ_{rot}) as the angular difference between the crystal orientations at smaller and larger strains for each grain. θ_{rot} in 706 grains during the first loading step (0%–1% strain) and θ_{rot} in 770 grains during the third loading step (2%–4% strain) are computed from the EBSD data (using the average orientation of each grain) and shown in Fig. 13 with respect to the area of each grain measured by EBSD. From 0% to 1% strain, θ_{rot} ranges from 0.5° to 2.5°. As shown in Fig. 13(a), the area of a grain has no apparent influence on θ_{rot} during the first loading step. From 2% to 4% strain, θ_{rot} ranges from 0° to 5.0°. As indicated by the red trend line in Fig. 13(b), grains of smaller size tend to have higher θ_{rot}. One explanation is that larger grains are more likely to have multiple active slip systems in different regions. The orientation rotations associated with different slip systems could partially nullify each other, thus reducing the overall orientation rotation for the whole grain.

Fig. 14 explores how θ_{rot} of each grain during the third loading step (2%-4% strain) is affected by the activated slip mode and the corresponding SF of the slip mode. For grains with single basal slip traces, those with high basal SF (0.4–0.5) tend to develop higher θ_{rot} than those with low basal SF (0.1–0.2). For grains with single prismatic or pyramidal I slip traces, they all have high SF (0.4–0.5) for the corresponding slip mode. On average, θ_{rot} in these grains are comparable with θ_{rot} in grains with basal slip trace and median basal SF (0.2–0.3). According to crystal plasticity theory (Roters et al., 2010), the plastic strain of a slip system depends on the ratio of τ^{α}/s^{α}, where τ^{α} and s^{α} are the resolved shear stress and CRSS, respectively, for the slip system α. Assuming that τ^{α} is proportional to

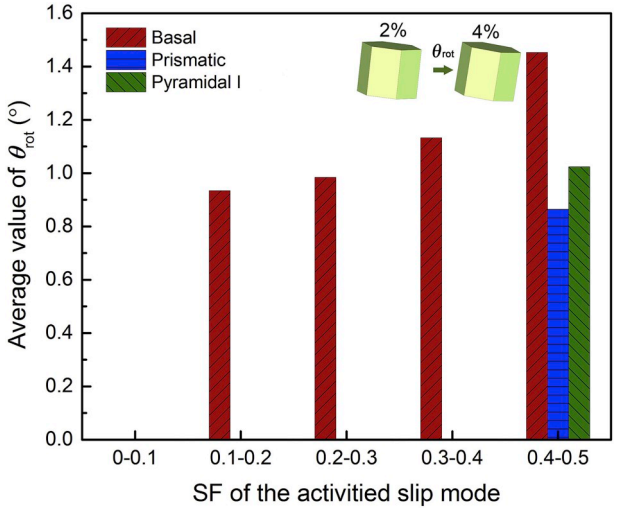

Fig. 14. Average θ_{rot} for grains dominated by different slip modes from 2% to 4%, binned by the SF of the corresponding slip mode.

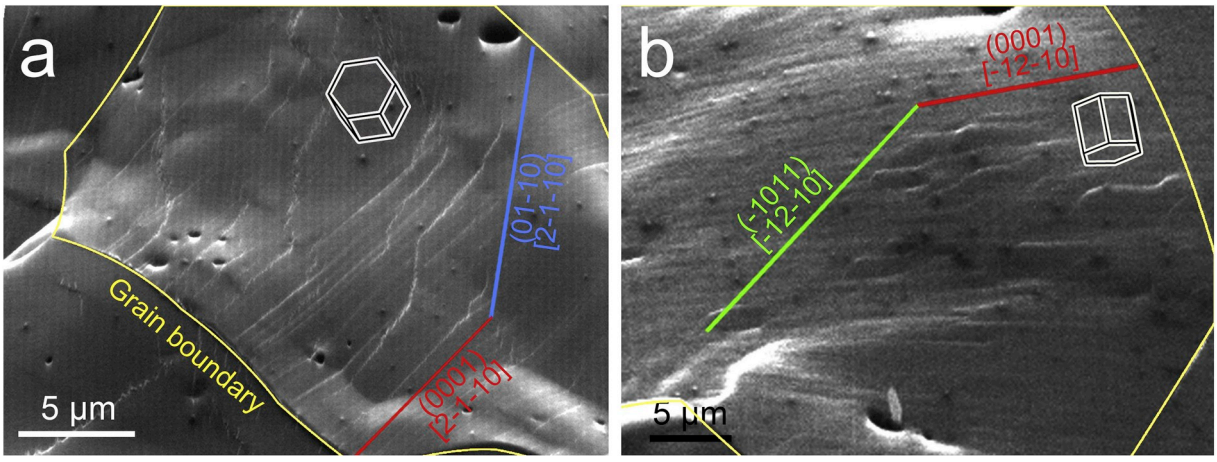

Fig. 15. Wavy slip lines observed during the in situ test at 8% strain: (a) cross-slip of < a > dislocations between basal and prismatic planes, (b) cross-slip of < a > dislocations between basal and pyramidal I planes.

the Schmid factor, we can roughly estimate the CRSS ratio between non-basal < a > slip (prismatic or pyramidal I < a >) and basal slip to be between 1.3 (= 0.4/0.3) and 2.5 (= 0.5/0.2). This range is consistent with the estimation obtained by slip trace analysis in Section 3.3.

4. Discussion

4.1. Non-basal slip and ductility of Mg alloys

Because basal slip can provide only two independent slip systems in Mg alloys, one effective way to improve the formability is to increase the activity of non-basal slip. Previous studies have shown that Y can promote both < c + a > and non-basal < a > slip activities (Sandlöbes et al., 2011; Zhang et al., 2016; Huang et al., 2018). For the Mg–0.47 wt% Ca alloy in this work, non-basal < a > slip was found to be active, and dislocation cross-slip was frequently observed between basal and non-basal planes, evidenced by wavy slip lines (Fig. 15(a and b)). This observation verifies the computational prediction by Yasi et al. (2012) that the addition of Ca would reduce the cross-slip barrier for < a > dislocations.

For pure Mg, the ratio of $CRSS_{non\text{-}basal}/CRSS_{basal}$ has been reported to be 40–100 for single crystals and 4–6 for polycrystals

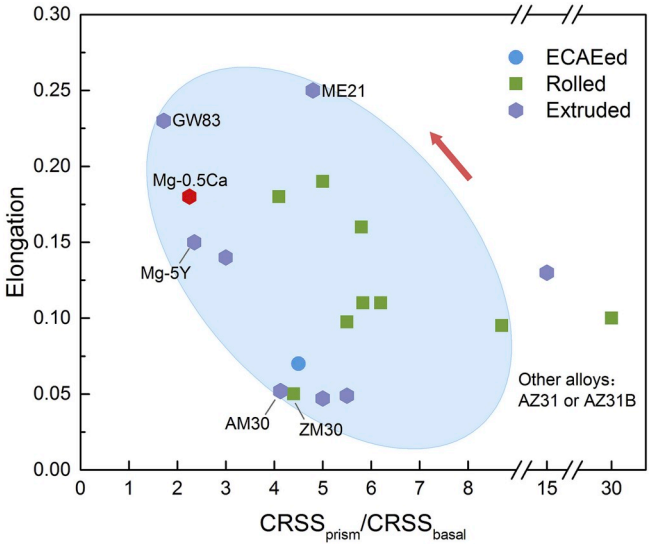

Fig. 16. Relation between the ratio of $CRSS_{prism}/CRSS_{basal}$ and tensile elongation for a variety of Mg alloys based on a literature survey and this work (Agnew et al., 2003, 2005, 2018; El Kadiri et al., 2013; Guo et al., 2015; Kabirian et al., 2015; Ma et al., 2017; Proust et al., 2009; Qiao et al., 2015; Sun et al., 2017; H. Wang et al., 2010a, 2013b, 2018a; Wu et al., 2012). ECAE is an abbreviation for equal channel angular extrusion.

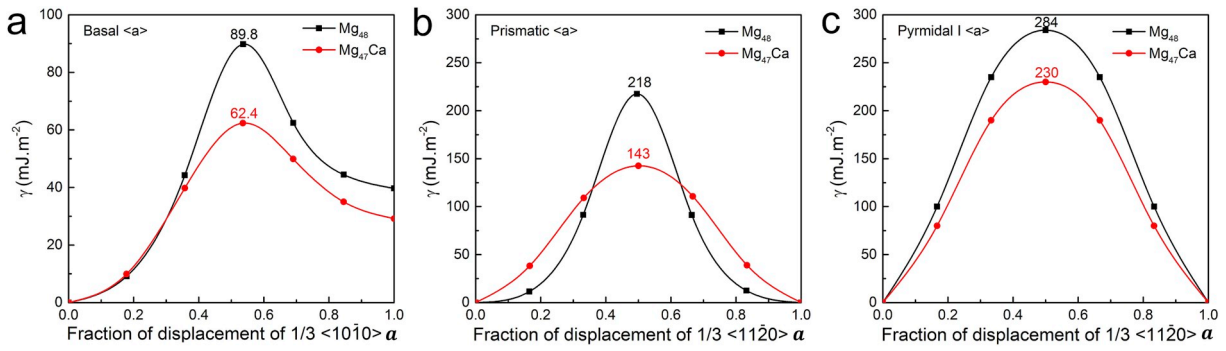

Fig. 17. GSFE curves for (a) basal slip, (b) prismatic slip, and (c) pyramidal I < a > slip in Mg_{48} and $Mg_{47}Ca$.

(Hutchinson and Barnett, 2010; Stanford and Barnett, 2013). For the Mg–0.47 wt% Ca alloy in this work, $CRSS_{prism}/CRSS_{basal}$ is found to be 1.9–2.6, which is much smaller than that for pure Mg. This ratio has an impact on the material ductility, as illustrated in Fig. 16, which explores the relationship between $CRSS_{prism}/CRSS_{basal}$ and tensile elongation for a variety of Mg alloys at room temperature. For the Mg–0.47 wt% Ca alloy, we simply use the average value of the upper and lower bounds ((1.9 + 2.6)/2 = 2.25) to represent its $CRSS_{prism}/CRSS_{basal}$ ratio. From Fig. 16, those Mg alloys with lower $CRSS_{prism}/CRSS_{basal}$ ratio tend to have larger tensile elongation.

In Ca-containing Mg ternary alloys such as Mg–1Al–0.1Ca (wt.%) (Sandlöbes et al., 2017) and Mg–0.3Zn–0.1Ca (wt.%) (Zeng et al., 2016a), pyramidal I or II < c + a > slip was identified in the deformed microstructure after 2% − 3% strain. The high ductility of these ternary alloys was attributed to the activation of pyramidal < c + a > slip. For the Mg–Ca binary alloy in this work, pyramidal < c + a > slip is less active, especially during early deformation. Compared to non-basal < a > slip, pyramidal < c + a > slip facilitates deformation along the c-axis of a grain. This may explain the higher ductility of Ca-containing Mg ternary alloys than that of the Mg–Ca binary alloy here.

4.2. Effect of Ca on the motion of non-basal dislocations

In order to understand why Ca can promote non-basal < a > slip, the GSFE (γ) curves along the faulting pathways for basal, prismatic, and pyramidal I < a > slips were calculated and plotted in Fig. 17. The addition of Ca reduces γ_{us} for all slip modes: basal slip from 89.9 mJ m^{-2} to 62.4 mJ m^{-2}, prismatic slip from 218 mJ m^{-2} to 143 mJ m^{-2}, and pyramidal I < a > slip from 284 mJ m^{-2} to 230 mJ m^{-2}. The calculated γ_{us} values are summarized in Table 3 and compared with some earlier works. For a planar dislocation core, such as basal slip, it is OK to use the derivative of γ ($-\nabla\gamma(u)$) as restoring force (τ) to estimate the Peierls stress against dislocation motion. However, the dislocation cores for non-basal slips are typically non-planar and tend to dissociate during the glide. Thus, simple calculation of τ with or without Ca is not useful to understand why non-basal slip is more active in Mg–Ca alloy. Instead, the interaction between the solute atom and the dislocation core must be computed. Using DFT, Yasi et al. (2012) predicted that Ca is one of the most effective elements (second only to Y) that can promote the cross slip of < a > dislocations from the basal plane to the prismatic plane. It is reasonable to assume that the cross slip can also occur onto the pyramidal I plane. This can explain the enhanced activity of non-basal < a > slip in Mg–Ca.

The effect of Ca on < c + a > dislocations has not been quantitatively assessed by DFT in the literature. Using the formulation in Ding et al. (2018), γ_{us} for < c + a > dislocations to glide on {10$\bar{1}$1} (pyramidal I) and {11$\bar{2}$2} (pyramidal II) planes were calculated for Mg and $Mg_{47}Ca$, and the result is shown in Table 3. Comparing the result of Mg and $Mg_{47}Ca$, γ_{us} for pyramidal I and II < c + a > slip are not reduced in relative to basal slip due to the presence of Ca. This can explains the low fraction of < c + a > slip in the Mg–Ca alloy. Nonetheless, the role of < c + a > dislocations in Mg's ductility should not be underestimated, as < c + a > slip provides a critical alternative to reduce local stress concentration when < a > dislocations cannot accommodate. Ductility improvement in Ca-containing Mg alloys is likely due to the combined effect of enhanced non-basal < a > slip in early deformation and some < c + a > slip in late deformation.

Table 3
Calculated values of γ_{us} for various slip modes. Literature values of γ_{us} are also shown for comparison.

Materials	γ_{us}^{Ba}(mJ·m^{-2})	γ_{us}^{Pri}(mJ·m^{-2})	$\gamma_{us}^{PyrI<a>}$(mJ·m^{-2})	$\gamma_{us}^{PyrI<c+a>}$(mJ·m^{-2})	γ_{us}^{PyrII}(mJ·m^{-2})
Mg (this work)	89.8	218	284	318	327
$Mg_{47}Ca$ (this work)	62.4	143	230	262	301
Mg (C. Wang et al., 2013a)	148	351	389	/	466
$Mg_{47}Ca$ (C. Wang et al., 2013a)	139	322	442	/	395
Mg (Yasi et al., 2009)	92	218	/	/	/

5. Conclusions

In this study, the deformation mechanisms of extruded polycrystalline Mg–0.47 wt% Ca alloy under tension were investigated by in situ EBSD. The main results are summarized as follows:

(1) Basal slip was the dominant deformation mechanism in this alloy at all strains, while prismatic and pyramidal I < a > slip became important after 2% strain. Non-basal < a > slip activity in this alloy was more pronounced than it was in Mg–2 wt.% Nd and AZ31 alloys under similar tensile strains. Pyramidal II < c + a > slip lines are occasionally found after 8% strain.
(2) The CRSS ratios between non-basal < a > and basal < a > slip were estimated by Schmid factor analysis. $CRSS_{prism}/CRSS_{basal}$ was estimated between 1.9 and 2.6, and $CRSS_{pyr\ I < a >}/CRSS_{basal}$ was estimated between 1.8 and 2.4. These ratios are consistent with the analysis of grain orientation rotation.
(3) Ca reduced the γ_{us} for all slip modes in Mg. The enhanced activity of non-basal < a > slip can be interpreted by Ca reducing the energy barrier for < a > dislocations to cross slip to non-basal planes.

Acknowledgements

This work is financially supported by the National Key Research and Development Program of China (No. 2016YFB0701203) and the National Natural Science Foundation of China (Nos. 51631006 and 51671127). We would like to thank Jian Wang for insightful discussions. We thank the Instrumental Analysis Center of Shanghai Jiao Tong University for the assistance in the FIB/TEM sample preparation. We also thank Beamline BL14B1 (Shanghai Synchrotron Radiation Facility) for providing the beam time and assistance during the experiments.

Appendix A. Supplementary data

Supplementary data to this article can be found online at https://doi.org/10.1016/j.ijplas.2019.04.020.

References

Aboulfadl, H., Deges, J., Choi, P., Raabe, D., 2015. Dynamic strain aging studied at the atomic scale. Acta Mater. 86, 34–42.
Agnew, S.R., Tomé, C.N., Brown, D.W., Holden, T.M., Vogel, S.C., 2003. Study of slip mechanisms in a magnesium alloy by neutron diffraction and modeling. Scripta Mater. 48, 1003–1008.
Agnew, S.R., Duygulu, Ö., 2005. Plastic anisotropy and the role of non-basal slip in magnesium alloy AZ31B. Int. J. Plast. 21, 1161–1193.
Agnew, S.R., Singh, A., Calhoun, C.A., Mulay, R.P., Bhattacharyya, J.J., Somekawa, H., Mukai, T., Clausen, B., Wu, P.D., 2018. In-situ neutron diffraction of a quasicrystal-containing Mg alloy interpreted using a new polycrystal plasticity model of hardening due to {10.2} tensile twinning. Int. J. Plast. 100, 34–51.
Aljarrah, M., Medraj, M., 2008. Thermodynamic modelling of the Mg–Ca, Mg–Sr, Ca–Sr and Mg–Ca–Sr systems using the modified quasichemical model. Calphad 32, 240–251.
Barkia, B., Doquet, V., Couzinié, J.P., Guillot, I., Héripré, E., 2015. In situ monitoring of the deformation mechanisms in titanium with different oxygen contents. Mater. Sci. Eng. A 636, 91–102.
Bian, M.Z., Sasaki, T.T., Nakata, T., Yoshida, Y., Kawabe, N., Kamodo, S., Hono, K., 2018. Bake-hardenable Mg-Al-Zn-Mn-Ca sheet alloy processed by twin-roll casting. Acta Mater. 158, 278–288.
Boehlert, C.J., Chen, Z., Gutiérrez-Urrutia, I., Llorca, J., Pérez-Prado, M.T., 2012. In situ analysis of the tensile and tensile-creep deformation mechanisms in rolled AZ31. Acta Mater. 60, 1889–1904.
Cepeda-Jiménez, C.M., Molina-Aldareguia, J.M., Pérez-Prado, M.T., 2015. Effect of grain size on slip activity in pure magnesium polycrystals. Acta Mater. 84, 443–456.
Cepeda-Jiménez, C.M., Prado-Martínez, C., Pérez-Prado, M.T., 2018. Understanding the high temperature reversed yield asymmetry in a Mg-rare earth alloy by slip trace analysis. Acta Mater. 145, 264–277.
Cottrell, A.H., Bilby, B.A., 1949. Dislocation theory of yielding and strain ageing of iron. Proc. Roy. Soc. A 62, 49–62.
Ding, Z., Liu, W., Sun, W., Li, S., Zhang, D., Zhao, Y., Lavernia, E.J., Zhu, Y., 2018. Origins and dissociation of pyramidal < c + a > dislocations in magnesium and its alloys. Acta Mater. 146, 265–272.
Dong, Q., Luo, Z., Zhu, H., Wang, L., Ying, T., Jin, Z., Li, D., Ding, W., Zeng, X., 2018. Basal-plane stacking-fault energies of Mg alloys: a first-principles study of metallic alloying effects. J. Mater. Sci. Technol. 34, 1773–1780.
El Kadiri, H., Baird, J.C., Kapil, J., Oppedal, A.L., Cherkaoui, M., Vogel, Sven C., 2013. Flow asymmetry and nucleation stresses of {10-12} twinning and non-basal slip in magnesium. Int. J. Plast. 44, 111–120.
Gu, X.N., Zheng, W., Cheng, Y., Zheng, Y.F., 2009. A study on alkaline heat treated Mg–Ca alloy for the control of the biocorrosion rate. Acta Biomater. 5, 2790–2799.
Guo, X.Q., Wang, H., Qiao, H., Mao, X.B., 2015. Numerical study of the large strain behavior of extruded magnesium alloy AM30 tube by elastic viscoplastic self-consistent model. Mater. Des. 79, 99–105.
Hofstetter, J., Rüedi, S., Baumgartner, I., Kilian, H., Mingler, B., Povoden-Karadeniz, E., Pogatscher, S., Uggowitzer, P.J., Löffler, J.F., 2015. Processing and microstructure–property relations of high-strength low-alloy (HSLA) Mg–Zn–Ca alloys. Acta Mater. 98, 423–432.
Huang, Z., Wang, L., Zhou, B., Fischer, T., Yi, S., Zeng, X., 2018. Observation of non-basal slip in Mg–Y by in situ three-dimensional X-ray diffraction. Scripta Mater. 143, 44–48.
Hutchinson, W.B., Barnett, M.R., 2010. Effective values of critical resolved shear stress for slip in polycrystalline magnesium and other hcp metals. Scripta Mater. 63, 737–740.
Imandoust, A., Barrett, C.D., Al-Samman, T., Inal, K.A., El Kadiri, H., 2017. A review on the effect of rare-earth elements on texture evolution during processing of magnesium alloys. J. Mater. Sci. 52, 1–29.
Kabirian, F., Khan, A.S., Gnäupel-Herlod, T., 2015. Visco-plastic modeling of mechanical responses and texture evolution in extruded AZ31 magnesium alloy for various loading conditions. Int. J. Plast. 68, 1–20.
Khosravani, A., Fullwood, D.T., Adams, B.L., Rampton, T.M., Miles, M.P., Mishra, R.K., 2015. Nucleation and propagation of {10-12} twins in AZ31 magnesium alloy. Acta Mater. 100, 202–214.
Kim, K.H., Jeon, J.B., Kim, N.J., Lee, B.J., 2015. Role of yttrium in activation of < c + a > slip in magnesium: an atomistic approach. Scripta Mater. 108, 104–108.
Kim, K.H., Hwang, J.H., Jang, H.S., Jeon, J.B., Kim, N.J., Lee, B.J., 2018. Dislocation binding as an origin for the improvement of room temperature ductility in Mg alloys. Mater. Sci. Eng. A 715, 266–275.

Kula, A., Jia, X., Mishra, R.K., Niewczas, M., 2016. Mechanical properties of Mg–Gd and Mg–Y solid solutions. Metall. Mater. Trans. B 47, 3333–3342.
Li, H., Mason, D.E., Bieler, T.R., Boehlert, C.J., Crimp, M.A., 2013. Methodology for estimating the critical resolved shear stress ratios of α-phase Ti using EBSD-based trace analysis. Acta Mater. 61, 7555–7567.
Ma, C., Chapuis, A., Guo, X.Q., Zhao, L.Y., Wu, P.D., Liu, Q., Mao, X.B., 2017. Modeling the deformation behavior of a rolled Mg alloy with the EVPSC-TDT model. Mater. Sci. Eng. A 682, 332–340.
Mendis, C.L., Oh-ishi, K., Ohkubo, T., Hono, K., 2011. Precipitation of prismatic plates in Mg–0.3Ca alloys with in additions. Scripta Mater. 64, 137–140.
Oh-ishi, K., Watanabe, R., Mendis, C.L., Hono, K., 2009. Age-hardening response of Mg–0.3at.%Ca alloys with different Zn contents. Mater. Sci. Eng. A 526, 177–184.
Pan, H., Ren, Y., Fu, H., Zhao, H., Wang, L., Meng, X., Qin, G., 2016. Recent developments in rare-earth free wrought magnesium alloys having high strength: a review. J. Alloy. Comp. 663, 321–331.
Pan, H., Yang, C., Yang, Y., Dai, Y., Zhou, D., Chai, L., Huang, Q., Yang, Q., Liu, S., Ren, Y., Qin, G., 2019. Ultra-fine grain size and exceptionally high strength in dilute Mg–Ca alloys achieved by conventional one-step extrusion. Mater. Lett. 237, 65–68.
Proust, G., Tomé, C.N., Jain, A., Agnew, S.R., 2009. Modeling the effect of twinning and detwinning during strain-path changes of magnesium alloy AZ31. Int. J. Plast. 25, 861–880.
Qiao, H., Angew, S.R., Wu, P.D., 2015. Modeling twinning and detwinning behavior of Mg alloy ZK60A during monotonic and cyclic loading. Int. J. Plast. 65, 61–84.
Roters, F., Eisenlohr, P., Hantcherli, L., Tjahjanto, D.D., Bieler, T.R., Raabe, D., 2010. Overview of constitutive laws, kinematics, homogenization and multiscale methods in crystal plasticity finite-element modeling: theory, experiments, applications. Acta Mater. 58, 1152–1211.
Sabat, R.K., Brahme, A.P., Mishra, R.K., Inal, K., Suwas, S., 2018. Ductility enhancement in Mg-0.2%Ce alloys. Acta Mater. 161, 246–257.
Sandlöbes, S., Zaefferer, S., Schestakow, I., Yi, S., Gonzalez-Martinez, R., 2011. On the role of non-basal deformation mechanisms for the ductility of Mg and Mg–Y alloys. Acta Mater. 59, 429–439.
Sandlöbes, S., Friák, M., Zaefferer, S., Dick, A., Yi, S., Letzig, D., Pei, Z., Zhu, L.-F., Neugebauer, J., Raabe, D., 2012. The relation between ductility and stacking fault energies in Mg and Mg–Y alloys. Acta Mater. 60, 3011–3021.
Sandlöbes, S., Friák, M., Korte-kerzel, S., Pei, Z., Neugebauer, J., Raabe, D., 2017. A rare-earth free magnesium alloy with improved intrinsic ductility. Sci. Rep. 7, 10458.
Seong, J.W., Kim, W.J., 2015. Development of biodegradable Mg–Ca alloy sheets with enhanced strength and corrosion properties through the refinement and uniform dispersion of the Mg_2Ca phase by high-ratio differential speed rolling. Acta Biomater. 11, 531–542.
Stanford, N., Barnett, M.R., 2013. Solute strengthening of prismatic slip, basal slip and {10Ī2}twinning in Mg and Mg–Zn binary alloys. Int. J. Plast. 47, 165–181.
Stanford, N., Cottam, R., Davis, B., Robson, J., 2014. Evaluating the effect of yttrium as a solute strengthener in magnesium using in situ neutron diffraction. Acta Mater. 78, 1–13.
Suh, B.C., Kim, J.H., Bae, J.H., Hwang, J.H., Shim, M.S., Kim, N.J., 2017. Effect of Sn addition on the microstructure and deformation behavior of Mg–3Al alloy. Acta Mater. 124, 268–279.
Sun, J., Jin, L., Dong, S., Dong, J., Zhang, Z., Wang, F., Ding, W., Luo, A.A., 2017. A combined electro backscattered diffraction and visco-plastic self-consistent analysis on the anisotropic deformation behavior in a Mg–Gd–Y alloy. Mater. Des. 122, 164–171.
Wang, C., Zhang, H.Y., Wang, H.Y., Liu, G.J., Jiang, Q.C., 2013a. Effects of doping atoms on the generalized stacking-fault energies of Mg alloys from first-principles calculations. Scripta Mater. 69, 445–448.
Wang, H., Boehlert, C.J., Wang, Q.D., Yin, D.D., Ding, W.J., 2016. In-situ analysis of the tensile deformation modes and anisotropy of extruded Mg-10Gd-3Y-0.5Zr (wt. %) at elevated temperatures. Int. J. Plast. 84, 255–276.
Wang, H., Wu, P.D., Gharghouri, M.A., 2010. Effects of basal texture on mechanical behaviour of magnesium alloy AZ31B sheet. Mater. Sci. Eng. A 527, 3588–3594.
Wang, H., Wu, P.D., Wang, J., Tomé, C.N., 2013b. A crystal plasticity model for hexagonal close packed (HCP) crystals including twinning and de-twinning mechanisms. Int. J. Plast. 49, 36–52.
Wang, H., Wu, P., Kurukuri, S., Worswick, M.J., Peng, Y., Yang, D., li, D., 2018a. Strain rate sensitivities of deformation mechanisms in magnesium alloys. Int. J. Plast. 107, 207–222.
Wang, L., Barabash, R.I., Yang, Y., Bieler, T.R., Crimp, M.A., Eisenlohr, P., Liu, W., Ice, G.E., 2011. Experimental characterization and crystal plasticity modeling of heterogeneous deformation in polycrystalline α-Ti. Metall. Mater. Trans. A 42, 626–635.
Wang, L., Huang, Z., Wang, H., Maldar, A., Yi, S., Park, J.-S., Kenesei, P., Lilleodden, E., Zeng, X., 2018b. Study of slip activity in a Mg-Y alloy by in situ high energy X-ray diffraction microscopy and elastic viscoplastic self-consistent modeling. Acta Mater. 155, 138–152.
Wu, P.D., Wang, H., Neale, K.W., 2012. On the large strain torsion of HCP polycrystals. Int. J. Appl. Mechanics. 4, 1250024.
Wu, Z., Curtin, W.A., 2015. The origins of high hardening and low ductility in magnesium. Nature 526, 62–67.
Wu, Z., Ahmad, R., Yin, B., Sandlöbes, S., Curtin, W.A., 2018. Mechanistic origin and prediction of enhanced ductility in magnesium alloys. Science 359, 447–452.
Xu, S.W., Oh-ishi, K., Kamado, S., Uchida, F., Homma, T., Hono, K., 2011. High-strength extruded Mg–Al–Ca–Mn alloy. Scripta Mater. 65, 269–272.
Yasi, J.A., Hector Jr., L.G., Trinkle, D.R., 2012. Prediction of thermal cross slip in magnesium alloys from a geometric interaction model. Acta Mater. 60, 2350–2358.
Yasi, J.A., Nogaret, T., Trinkle, D.R., Qi, Y., Hector Jr., L.G., Curtin, W.A., 2009. Basal and prism dislocation cores in magnesium: comparison of first-pinciples and embedded-atom-potential methods predictions. Model. Simulat. Mater. Sci. Eng. 17, 055012.
Yang, T.Y., Wen, W., Yin, G.Z., Li, X.L., Gao, M., Gu, Y.L., Li, L., Liu, Y., Lin, H., Zhang, X.M., Zhao, B., Liu, T.K., Yang, Y.G., Li, Z., Zhou, X.T., Gao, X.Y., 2015. Introduction of the X-ray diffraction beamline of SSRF. Nucl. Sci. Tech. 26, 1–5.
Zeng, Z.R., Bian, M.Z., Xu, S.W., Davies, C.H.J., Birbilis, N., Nie, J.F., 2016a. Effects of dilute additions of Zn and Ca on ductility of magnesium alloy sheet. Mater. Sci. Eng. A 674, 459–471.
Zeng, Z.R., Zhu, Y.M., Xu, S.W., Bian, M.Z., Davies, C.H.J., Birbilis, N., Nie, J.F., 2016b. Texture evolution during static recrystallization of cold-rolled magnesium alloys. Acta Mater. 105, 479–494.
Zhang, B., Wang, Y., Geng, L., Lu, C., 2012. Effects of calcium on texture and mechanical properties of hot-extruded Mg–Zn–Ca alloys. Mater. Sci. Eng. A 539, 56–60.
Zhang, D., Wen, H., Arul Kumar, M., Chen, F., Zhang, L., Beyerlein, I.J., Schoenung, J.M., Mahajan, S., Lavernia, E.J., 2016. Yield symmetry and reduced strength differential in Mg–2.5Y alloy. Acta Mater. 120, 75–85.